JTTEE5 20:12–20
DOI: 10.1007/s11666-010-9554-4
1059-9630/$19.00 © ASM International

Velocity Diagnostics for Gas Velocity Distributions in Cold Gas and Plasma Spraying Using Non-Resonant Laser Scattering

Sebastian Lange, Marco Sieber, Günter Forster, José Luis Marqués-López, Jochen Schein, and Christian J. Kähler

(Submitted May 3, 2010; in revised form July 14, 2010)

In cold spray and thermal spray applications, one of the primary factors affecting coating deposition is the location where particles are injected into the gas jet. Therefore, a detailed knowledge of the gas flow distribution at that location is required. Use of non-resonant laser scattering allows to spatially resolve the distribution of drift velocity and mass density within the flow, particularly, at locations close to the injector. Based on this technique, this article presents a new diagnostic to locally measure drift velocity and relative mass density distribution of a gas stream. Its application is mainly focused on cold gas flows, where velocity measurements in a supersonic nozzle, obtained by means of laser scattering correlate well with theoretical calculations and particle image velocimetry (PIV) experimental results.

Keywords diagnostics, Fizeau interferometer, gas velocity, laser scattering, particle imaging velocimetry, supersonic flow

1. Introduction

Thermal spraying is one key technology of material science. However, despite all efforts uncontrolled deviations arise in the quality of coatings deposited by means of thermal spray. Thus, knowledge of the fundamental physics involved in thermal spraying needs to be improved in order to achieve reproducible spraying conditions. Implementing this knowledge into numerical models based on reliable experimental data is currently pursued (Ref 1). The development of a diagnostic tool to provide some of these data is the subject of this article.

This article is an invited paper selected from presentations at the 2010 International Thermal Spray Conference and has been expanded from the original presentation. It is simultaneously published in *Thermal Spray: Global Solutions for Future Applications, Proceedings of the 2010 International Thermal Spray Conference*, Singapore, May 3-5, 2010, Basil R. Marple, Arvind Agarwal, Margaret M. Hyland, Yuk-Chiu Lau, Chang-Jiu Li, Rogerio S. Lima, and Ghislain Montavon, Ed., ASM International, Materials Park, OH, 2011.

Sebastian Lange, Marco Sieber, Günter Forster, José Luis Marqués-López, and **Jochen Schein**, Department of Electrical Engineering, Universität der Bundeswehr München, Werner-Heisenberg-Weg 39, 85577 Neubiberg, Germany; and **Christian J. Kähler**, Department of Aerospace Engineering, Universität der Bundeswehr München, Werner-Heisenberg-Weg 39, 85577 Neubiberg, Germany. Contact e-mails: s.lange@unibw.de and jochen.schein@unibw.de

Particle-based velocimetry is a well-established method to determine flow velocities in fluid mechanics (Ref 2). This work describes a non-particle-based method to measure the drift velocity of fast gas flows based on laser scattering. Such technique can be applied to thermal flows that cannot tolerate contamination of the gas flow due to the use of tracer particles. Non-resonant scattering has been used in science since the mid-1970s (Ref 3, 4). Optical techniques based on light scattering have been developed for different kinds of measurements such as density and temperature (Ref 4, 5) or velocity (Ref 6). Since the mid-1990s measurement methods for estimating dynamic physical patterns have been established (Ref 7, 8).

Based on well-known (Ref 6-12) scattering techniques, a faster and more stable experiment has been developed to measure drift velocity and relative density distribution within a flow.

In principle two methods for analysis of scattered spectra are known (Ref 8, 10), either the spectrum is resolved with expensive monochromators or with high resolution optical filters such as a Fabry-Perot interferometer (FPI). For such filters two different techniques are established: the scanning and the static mode. In the first mode the optical arrangements are changed during a complete measurement and the scattered spectrum is scanned point wise. In the static mode temperature, density, and velocity are determined accordingly to theoretically calculated spectra (Ref 13). The applied technique in this article corresponds to the static type and allows the measurement of drift velocities within fast gas flows without any theoretically calculated data or changes in the optical arrangement of the experiment itself. Due to the fundamental modification in the basic geometry of the interferometer, knowledge of the scattered spectra is not necessary.

This article is organized as follows. A short overview of the theoretical basis is given in the next section. The subsequent section describes the three experimental set-ups. In section 4, an error analysis is discussed. Results are presented in the fifth section. An outlook for further implementation is given in the section 6 and a conclusion in section 7.

2. Theory

2.1 Doppler Shift

The dipole approximation is a useful method to describe non-resonant light scattering effects (Ref 14, 15). A charge in motion, assumed to be an electron from here on, interacts with electromagnetic radiation (EMR), e.g., a laser beam. For non-relativistic velocities the influence of the magnetic field component is negligible. The external electric field induces a periodic motion on the electron and this oscillating electron emits itself an EMR with the same wavelength as the incident electric field. The radiation pattern of the electron is that of a Hertzian dipole. The efficiency of the scattering process can be described by its differential scattering cross section. This cross section is the ratio of the scattered Poynting vector at the point of observation (PO) to the Poynting vector of the external EMR times the squared distance between the PO and the point where the scattering (PS) takes place. If the electron is bound inside an atom or molecule the energy binding the electron to its nucleus has to be taken into account in the scattering cross section. This scattering process is called Rayleigh scattering. For free electrons the binding energy vanishes and the scattering process is called Thomson scattering. In cold gas flows there are nearly no free electrons and thus Rayleigh scattering dominates.

An optical Doppler shift occurs if the velocity vector $\vec{v}_{\mathrm{Drift}}$ of the electron has a component parallel to the electric field of the incident EMR $\vec{S}_{1\mathrm{st}}$, Fig. 1. The wavelength of the scattered EMR $\vec{S}_{\mathrm{scat}}$ is given by

$$\lambda_1 = \lambda_0 \sqrt{\frac{c - v_{\mathrm{Drift}} \sin(\Phi)}{c + v_{\mathrm{Drift}} \sin(\Phi)}},$$

where 90-Φ describes the angle between the direction of the drift velocity and Poynting's vector of the incident

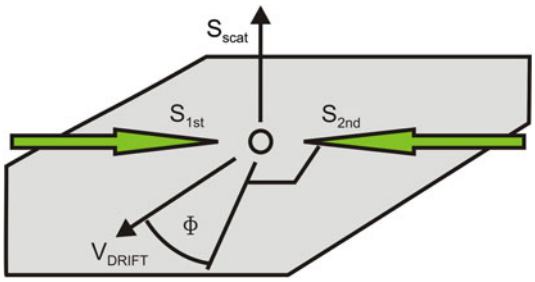

Fig. 1 Scattering geometry for the experiment, where the light scattered from $\vec{S}_{1\mathrm{st}}$ is slightly blue shifted (toward smaller wavelength) and the light scattered from $\vec{S}_{2\mathrm{nd}}$ is slightly red shifted

EMR, λ_0 describes the wavelength of the incident EMR and c is the speed of light. To improve accuracy the wavelength shift is measured relative to that induced by a second EMR $\vec{S}_{2\mathrm{nd}}$. The second EMR has the opposite direction of the first EMR, thus the wavelength of the scattered EMR is

$$\lambda_2 = \lambda_0 \sqrt{\frac{c + v_{\mathrm{Drift}} \sin(\Phi)}{c - v_{\mathrm{Drift}} \sin(\Phi)}}.$$

If both external EMR's have the same wavelength λ_0 then the relative wavelength shift between both scattered EMR's is given by:

$$\Delta\lambda = \lambda_1 - \lambda_2 \approx 2\lambda_0 \frac{v_{\mathrm{Drift}}}{c} \sin(\Phi). \qquad \text{(Eq 1)}$$

The measured spectrum at the detector is the sum of all scattering events within the scattering volume; therefore, the density distribution inside this volume has a significant influence on the total spectrum (Ref 6, 15). Optoacoustics effects, induced by the interaction of the electrons with the scattered EMR's, cannot be resolved by the developed interferometer and thus will not be considered for data analysis.

2.2 Interferometer

The small wavelength shift induced by the drift motion of the gas flow is measured by a modified FPI. A classical FPI consist of two parallel mirrors with a high reflection factor R spaced within a distance d. If the direction of propagation of the incident monochromatic EMR is perpendicular to the parallel mirrors multi-beam interference causes a transmitted intensity distribution described by an Airy profile (Ref 16)

$$S(\lambda, d) = \frac{1}{1 + 4\frac{R}{(1-R)^2} \sin^2\left(2\pi\frac{d}{\lambda}\right)}. \qquad \text{(Eq 2)}$$

This profile approximately corresponds to a periodic sequence of Lorentzian functions and reaches maxima for $2(d/\lambda) = k$, with k being an integer number (Ref 16-20). The distance between two consecutive maxima is called free spectral range (FSR) and is given by

$$\left|2\frac{d}{\lambda^2}\Delta\lambda\right| = \Delta k = 1 \Rightarrow \mathrm{FSR} = |\Delta\lambda| = \frac{\lambda^2}{2d}. \qquad \text{(Eq 3)}$$

The influence of the drift velocity to the corresponding interference pattern of an FPI is shown in Fig. 2.

The resolving power of an FPI is correlated to the full width at half maximum (FWHM) of the corresponding Lorentzian function. If the wavelength difference between two monochromatic EMR's is smaller than 10^{-3} nm, the length scale derived from $\mathrm{FWHM} = 4\left((1-R)/\left(\sqrt{4R}\right)\right)$, a separation of the corresponding spectra is not possible. In our application, the expected wavelength shift is smaller than the resolution of the available traditional FPI. The use of higher reflective mirrors is not recommended because not only the thermal stability of the FPI becomes

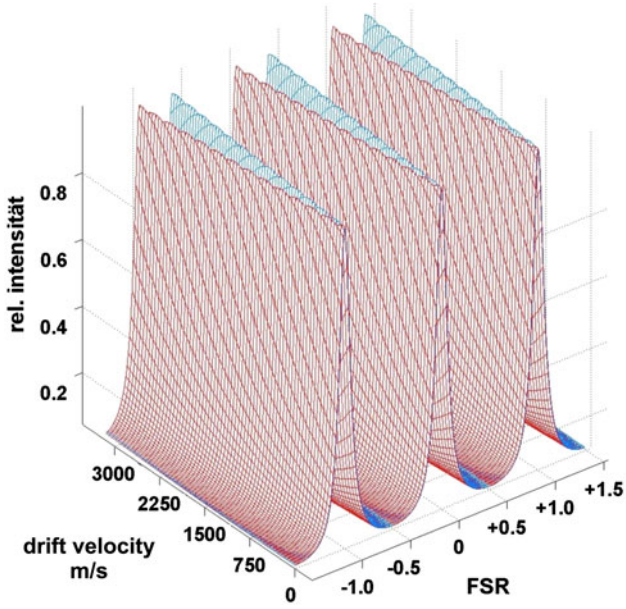

Fig. 2 Influence of the drift velocity on the FSR corresponding to the Airy profile for the scattered laser 1 (blue shifted) and the scattered laser 2 (red shifted)

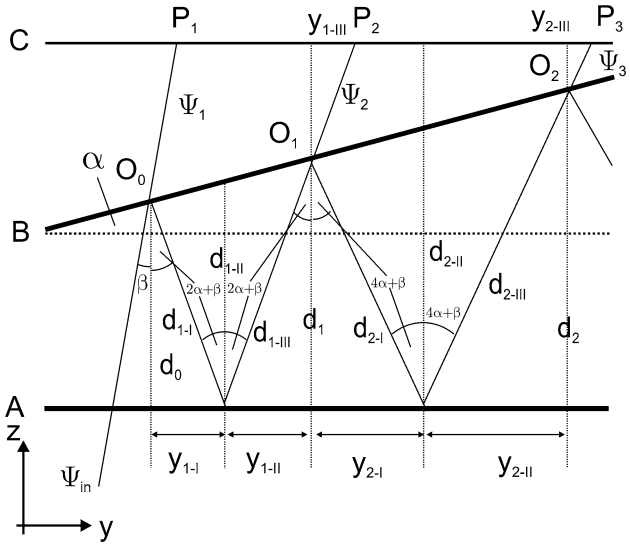

Fig. 3 Basic geometry of the modified interferometer

affected, but also the transmitted intensity decreases. To circumvent these problems the new interferometer features a second mirror B, which is slightly tilted by a small angle $\alpha \approx 0.01°$. The basic geometry of the used interferometer is shown in Fig. 3.

The amplitude of a monochromatic linearly polarized wave is represented by $\underline{\Psi} = E\exp(-j\phi)$, where ϕ denotes the phase and E is the amplitude of the electric field. Assuming that the used mirrors are thin and absorption effects are negligible, the sum of the amplitude of transmitted and reflected EMR is the amplitude of the incoming EMR. The angle of incidence between the EMR perpendicular to the first plate A and the incoming monochromatic EMR $\underline{\Psi}_0$ is β. Due to the fact that both angles are small the influence of such angles to the transmission factor is negligible. The transmitted EMR penetrates the second plate at point O_0 under an angle $\alpha+\beta$ and both effects are iteratively repeated. The transmitted EMR can be written as $\Psi_1 = \sqrt{T^2}\Psi_0\exp(j\delta_1)$. The distance between the point where the EMR enters the interferometer and the point P_1 at the plane of observation

$$d_{\text{sum}} = d_{\text{in}} + d_{\text{out}} = \frac{d_0}{\cos(\beta)} + \frac{\overline{AC} - d_0}{\cos(\beta)}$$

induces a phase δ_1.

The amplitude of the twice reflected and then transmitted EMR at the point P_2 is $\Psi_2 = TR\Psi_0\exp(j\delta_2)$. The phase δ_2 is induced by the sum of the distances inside the interferometer $d_{\text{in}} = \frac{d_0}{\cos(\beta)} + d_{1-\text{I}} + d_{1-\text{III}}$ and outside $d_{\text{out}} = \frac{\overline{AC}-d_1}{\cos(2\alpha+\beta)}$. At the point P_n a $m = n^2$-times reflected and then transmitted EMR yields $\underline{\Psi}_n = R^n T\underline{\Psi}_0\exp(j\delta_n)$. The phase δ_n is induced by the distance

$$d_{\text{sum},n} = \frac{d_0}{\cos(\beta)} + \sum_{i=1}^{n}(d_{i-\text{I}} - d_{i-\text{III}}) + \frac{\overline{AC} - d_n}{\cos(2n\alpha+\beta)}.$$

The resulting amplitude at this point is given by (Eq 4)

$$\underline{\Psi}_{\text{sum}} = T\underline{\Psi}_0\left[\exp(j\delta_1) + R\exp(j\delta_2) + R^2\exp(j\delta_3) + \cdots\right]$$
$$\underline{\Psi}_{sum} = T\underline{\Psi}_0\sum_{i=0}^{n} R^i\exp(j\delta_{i+1}) \qquad \text{(Eq 4)}$$

Due to the fact that the induced phase of all interacting EMR's is a function of the travelled distance a closed analytic solution is not possible. According to Ref (21-23), the interference pattern at the plane of observation can be calculated numerical. For a given error of relative intensity ΔI the number N EMR's interfering with each other can be estimated as

$$N \approx \frac{\log(\Delta I)}{2\log(R)}.$$

For a reflection coefficient of $R = 0.8$ and an error of $\Delta I \leq 1\%$ this equation leads to $N \approx 10$. The corresponding interference pattern (red) for the original laser, a wavelength of $\lambda = 532$ nm and a minimum plate separation of (a) $d = 6.4$ mm and (b) $d = 1.97$ mm, respectively, differs from the Airy Profile of an ideal FPI as shown in Fig. 4. The more symmetric (smaller intensity) line represents the calculated interference pattern for an air flow with a temperature of $T = 300$ K. The resulting maximum of the intensity decreases with an increasing temperature. The resulting intensity of the filtered spectrum is 72% for a minimum distance of $d = 6.4$ mm but still 90% for $d = 1.97$ mm, thus for higher temperatures the distance between both mirrors has to be reduced. It is worth noting that with the distance used at the moment $d = 6.4$ mm flows with temperatures up to 4000 K can be evaluated.

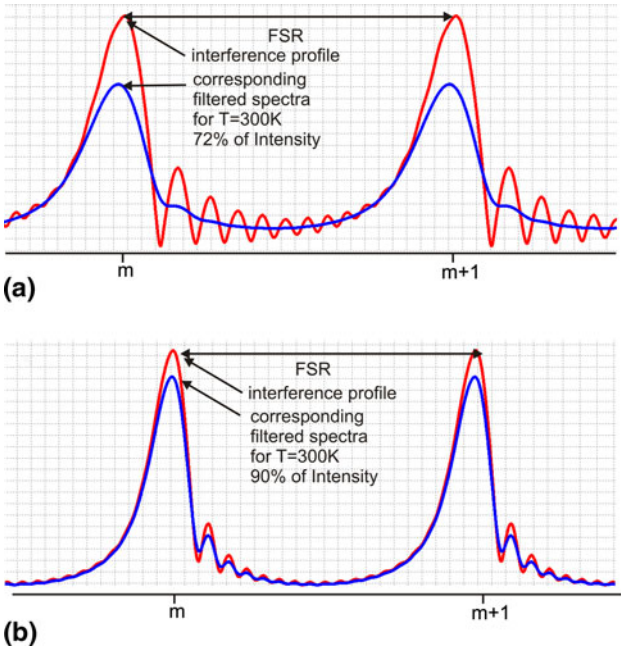

Fig. 4 Calculated interference profile for the original laser and for the laser scattered at an air flow with a temperature of $T = 300$ K (small intensity) for minimum plate seperation of (a) $d = 6.4$ mm and (b) $d = 1.97$ mm, respectively

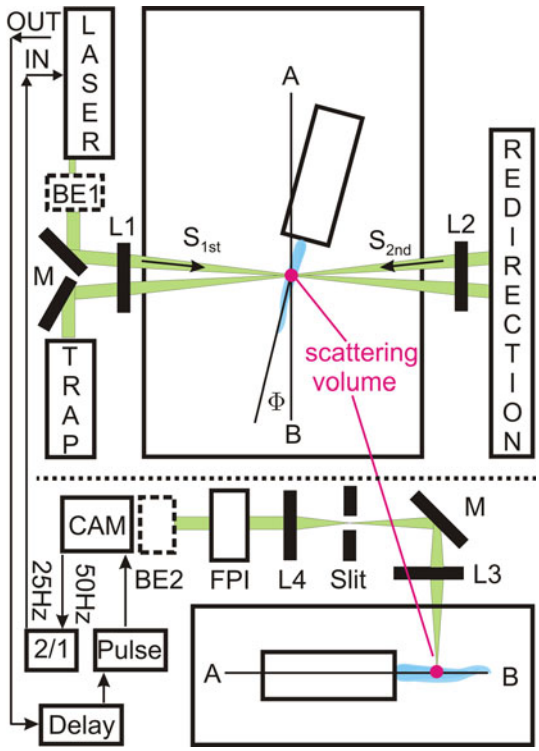

Fig. 5 Experimental setup (top) irradiation and (below) detection part

3. Experimental Setup

A Nd-YAG laser system (Coherent™ Infinity™) is the source of the external EMR.

This system uses an internal frequency doubling crystal and provides a 3 ns pulse FWHM. The setup can be divided into an irradiating and a detecting part. Both parts are schematically shown in Fig. 5. Three different setups were developed in order to find systematic errors. Different nozzles were positioned on a three stepper positioning system inside a chamber with controlled atmosphere. To provide better thermal stability all optical components were situated outside the chamber. To improve the lifetime of all optical components as well as to minimize the scattering volume a beam expander (BE1) was installed inside the irradiating part to increase the beam diameter by a factor of 2 thus reducing the intensity of the incident radiation by a factor of 4.

After passing several apertures to minimize stray light laser beam $\vec{S}_{1st}$ is focused onto a location inside the flow using a converging lens L1 ($f = 500$ mm), with the incident beam directed at an angle against the direction of the flow resulting in the light being scattered by the flow to be shifted toward shorter wavelengths. The converging lens L2 parallelizes the expanding beam, which after having been reflected at six mirrors is redirected back into the flow. The beam $\vec{S}_{2nd}$ is focused by L2 onto the same scattering volume as beam $\vec{S}_{1st}$, this time partially directed along the flow (red-shifted scattered light). After that the beam, after crossing L1 again, is directed into a light trap. The additional optical path between $\vec{S}_{1st}$ and $\vec{S}_{2nd}$ is 4 m, which induces a delay of approximately 13 ns between the blue- and the red-shifted signal.

The converging lens L3 collects the scattered photons, emitted perpendicularly to the gas flow plane and a high precision slit placed in the focal plane of L3 is used to image the scattering volume. Converging lens L4 parallelizes the scattered EMR and maps it through the interferometer onto the CCD chip of an intensified MCP-CCD camera. The objective and an additional beam expander BE2 are adjusted in the camera and focussed onto the second mirror of the used interferometer. BE2 is installed to increase the active area of the CCD chip used. The 50 Hz video output of the camera is used as an external trigger for the laser system. Employing an external delay and pulse generator the Q switch signal of the laser system in turn provides a trigger signal for the shutter of the camera operating at exposure times of 10 ns. This time adjustment allows for a defined distinction between the recording of the scattered light produced by each of the two laser beams. The scattering volume is in the order of $200 \times 200 \times 200$ μm^3.

Three different setups were used with slight variations in the optical arrangement. To speed up the experiment by decreasing the CCD area that needs to be analyzed, BE2 is removed in the second and third setup. In addition, BE 1 was removed increasing the intensity of the scattered light thus reducing the number of events that need to be acquired.

For an accurate determination of the wavelength shift, not only the scattered light from the two separated beams

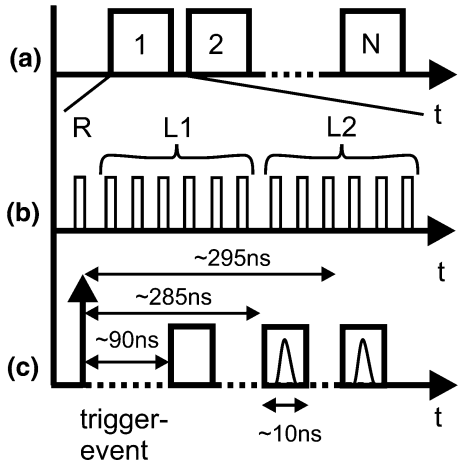

Fig. 6 (a) Time sequence of a whole measurement of *N* cycles. (b) Each cycle consisting of a reference and several measurements for the two scattered beams. (c) Distribution of delay events

is required, but also reference pictures without laser beam. The recording procedure consists of six consecutive pictures for the first beam, followed by six reference pictures (without beam) and six further pictures for the second beam, Fig. 6(b). The timing diagram of a cycle can be described as follows: (i) the delay time is set to $t_{\text{delay}} \approx 90 \times 10^{-9}$ s and pictures containing no scattering events (without laser) are taken to be used as reference; (ii) the delay time is set to $t_{\text{delay}} \approx 285 \times 10^{-9}$ sand pictures containing scattering events of the first incident beam are stored. And (iii) the delay time is set to $t_{\text{delay}} \approx 295 \times 10^{-9}$ s and pictures containing scattering events from the second beam are obtained, Fig. 6(c). This procedure will be repeated until the calculated cycle number *N* is reached, Fig. 6(a). All pictures are digitalized with a frame grabber and the digital outputs are used to drive the delay generator. The weak scattering process can be affected by two kinds of disturbances: either scattering from heavy dust particles or an electric breakdown inside the flow produced by the laser pulse. Both effects lead to an event of much higher intensity at the detector compared to the intensity of the scattering process and can be sorted out easily.

The remaining pictures of the first beam are integrated and the reference pictures are treated analogously; the latter are subtracted from the former. The same procedure is used for the second beam. The results for the first and second beam rescaled to their respective maximum are shown in Fig. 7. The bright lines represent the maxima of the filtered spectra and the distance between two consecutive maxima corresponds to the FSR.

For every maximum a region of interest (ROI) is defined. To obtain the relative wavelength shift a mathematical description of those maxima corresponding to the same order of interference for each scattered beams has to be evaluated. Assuming that the profiles of a filtered EMR with temperature *T* are of Lorentzian shape, such a distribution is fitted to the resulting intensity width

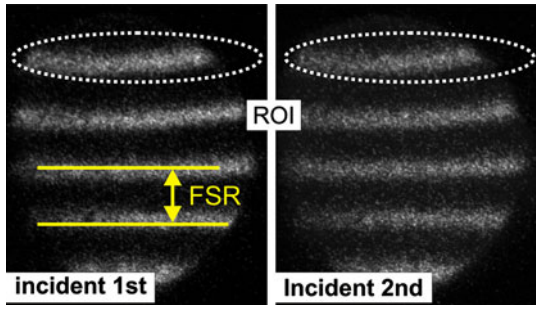

Fig. 7 Filtered scattered spectra re-scaled to respective maximum with region of interest (ROI) and FSR

at each column in a ROI. The position of the Lorentzian maximum for each column is used to fit a second order polynomial to describe the possible curvature of the maximum bands. The distance p_i between the respective fits for the first and second beam represents the relative distance in Pixel for this ROI. The averaged distance for all *N*ROI's $d_{\text{Pixel}} = \frac{1}{N}\sum_{i=1}^{N} p_i$ and for the FSR in pixel $\text{FSR}_{\text{Pixel}}$ lead to the relative wavelength shift $\Delta\lambda = \frac{d_{\text{Pixel}}}{\text{FSR}_{\text{Pixel}}}\text{FSR}$. Once the scattering geometry is known the wavelength shift correlates directly to the gas drift velocity according to (5)

$$v_{\text{Drift}} = \frac{\Delta\lambda}{2\lambda_0 \sin(\Phi)} c. \qquad \text{(Eq 5)}$$

4. Uncertainty Analysis

Rayleigh scattering is a process with small cross sections thus producing small signal levels. Therefore, measurement uncertainties are often limited by photon statistical noise, which can be approximately described as a Poisson process. The variance of a Poisson statistical process is determined by the mean number of photons detected. The number of photons per picture is given by:

$$N_{\text{R}} = \varepsilon \frac{E_0 d_{\text{Slit}} \lambda n_{\text{L}} \Omega}{hc} \frac{d\sigma}{d\Omega}, \qquad \text{(Eq 6)}$$

where ε describes the quantum efficiency factor, E_0 is the pulse energy, d_{Slit} is the width of the precision slit in the focal plane of L3, λ is the wavelength of the laser, n_{L} is the gas number density for air, Ω is the solid collection angle, *h* is the Planck's constant and $d\sigma/d\Omega$ is the differential scattering cross section. The lower bound of uncertainty for the drift velocity of a Gaussian Rayleigh spectrum is $\sigma_{\text{Drift}} = \sqrt{k_{\text{B}} T / m N_{\text{R}}}$ (Ref 8). In this equation, k_{B} is Boltzmann's constant, *T* is the temperature, and *m* is the molecular mass. With temperatures of 170 and 300 K, respectively, and 667 pictures per channel per measurement the lower bound of uncertainties for the estimated drift velocity is 0.2-0.3 m/s. It is worth noting that the lower bound does not depend on the velocity but on the temperature and therefore the relative error decreases with increasing velocities and decreasing temperature.

For the experiment discussed the estimation of the core area of a Lorentzian line profile is given by (Ref 20):

$$\delta\sigma_C = 1.11\sigma_W/\sqrt{N_R}, \quad \text{(Eq 7)}$$

where σ_W is the measured width of the corresponding Lorentzian profile. For the uncertainty analysis, this effect and the uncertainty of the scattering angle were taken into account. For characteristic parameters and a relative error of 10% the minimum velocity to be 88 m/s. To minimize the relative error the number of obtained pictures per channel or the width of the high precision slit in the focal plane of L3 has to be increased. Nevertheless, increasing the number of pictures leads to a decreased thermal stability during a measurement and an increased slit width leads to a reduction of the spatial resolution and thus measurements at the same point will be repeated and the results averaged.

5. Results

Experiments are performed employing subsonic and supersonic nozzles. For the sake of brevity only the results of the supersonic experiments are described. A supersonic Laval nozzle (Ma = 2.2, v = 550 m/s) was designed and built (Fig. 8).

The contour of the nozzle was calculated according to the Foelsch estimation (Ref 24), velocity measurements were performed using a PIV system, detecting small entrained particles as well as laser scattering. Results measured with the particle image velocimetry (PIV) technique are slightly lower than the expected ones, although the deviations are within the manufacturing tolerance of the nozzle, Fig. 9(a).

Results for all three experimental setups show a strong correlation between the velocities determined by laser scattering and the velocities obtained with means of PIV. Velocity distributions measured with the second setup for transversal sections at 8.5 and 11 mm from the nozzle outlet are shown in Fig. 9(b), (c) compared to the PIV results at the same transversal sections. Both distributions agree well with the corresponding PIV results.

The small spatial resolution of the PIV system and the extreme sensitivity to the scattering angle, which can only be determined within certain limits (~1°) are possible sources for the deviation between both results. For the chosen scattering angle of ~25° this uncertainty leads to a relative error of ~5%. Results obtained by the PIV technique represent the averaged velocities of the injected particles ($\varnothing \simeq 0.5$ µm) dragged by the flow within a

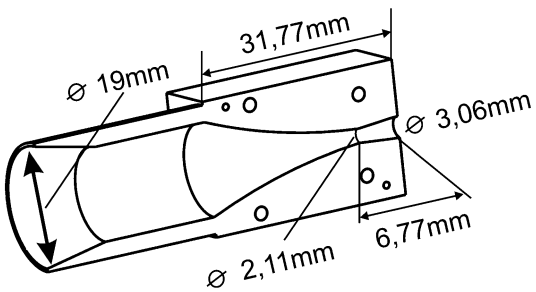

Fig. 8 Schematic of the supersonic nozzle with an outlet Mach number of 2.25

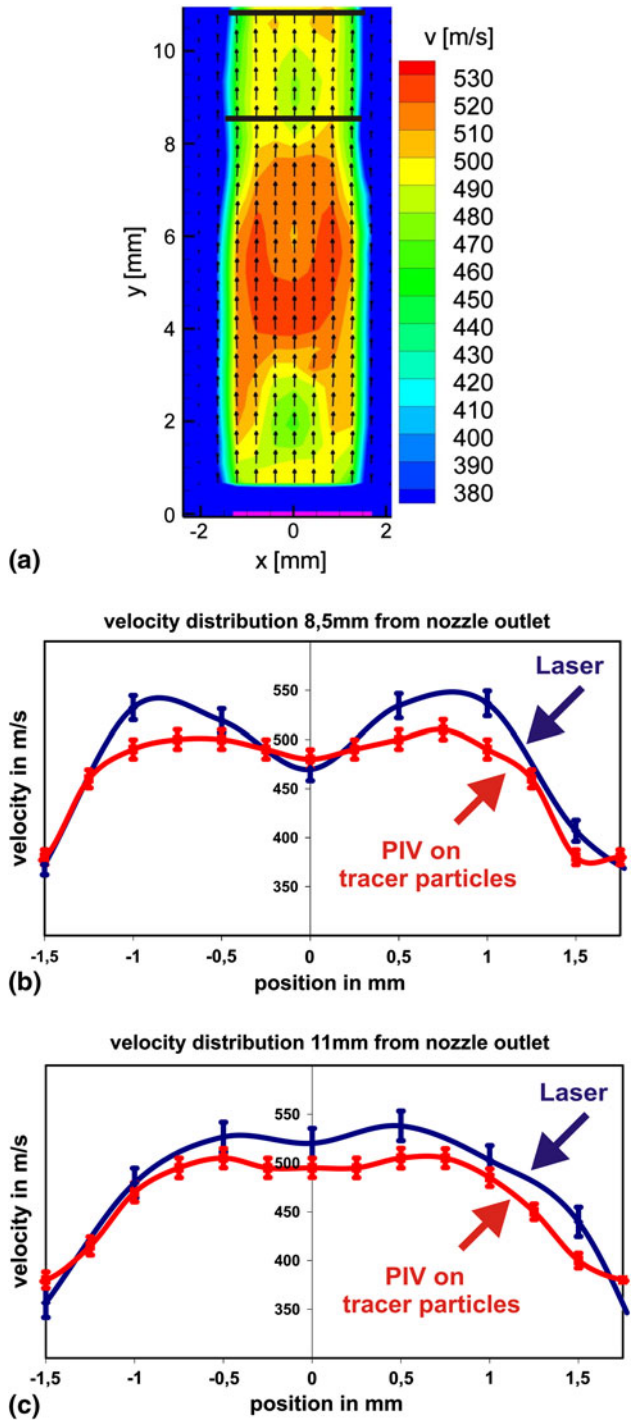

Fig. 9 (a) Velocity distribution of the supersonic nozzle measured by means of PIV. Velocity distribution measured by means of laser scattering compared to PIV, both at a transversal section, (b) 8.5 mm downstream from the nozzle outlet, and (c) 11 mm downstream the nozzle

volume of $200 \times 400 \times 1000\ \mu m^3$; whereas velocities obtained by means of laser scattering represent the averaged velocity within the scattering volume, which is about an order of magnitude smaller, resulting in a deviation of the two results.

The spatial resolution for the experiment is further limited by the width ($d_{Slit} = 0.2$ mm) of the high precision slit in the focal plane of L3. The error bars represent the calculated standard deviation for the chosen experiment, incorporating the described analysis. It is worth noting that stray light leads to a smaller detected wavelength shift and thus to a smaller velocity.

In addition, the experiment provides also the possibility to measure a relative density distribution since the intensity at the PO correlates directly to the number of scattering electrons. However, a determination of the absolute density is not possible because the absolute temperature corresponding to the scattered spectrum cannot be determined. In order to validate the relative density distribution obtained by laser scattering, the Schlieren technique has been used, a transversal section 10 mm from the nozzle has been selected, since the density gradients are very pronounced at such location. The density profile at this location, measured with the laser scattering technique, compares well to that obtained from the Schlieren measurement, Fig. 10. Again, two different techniques show good agreement.

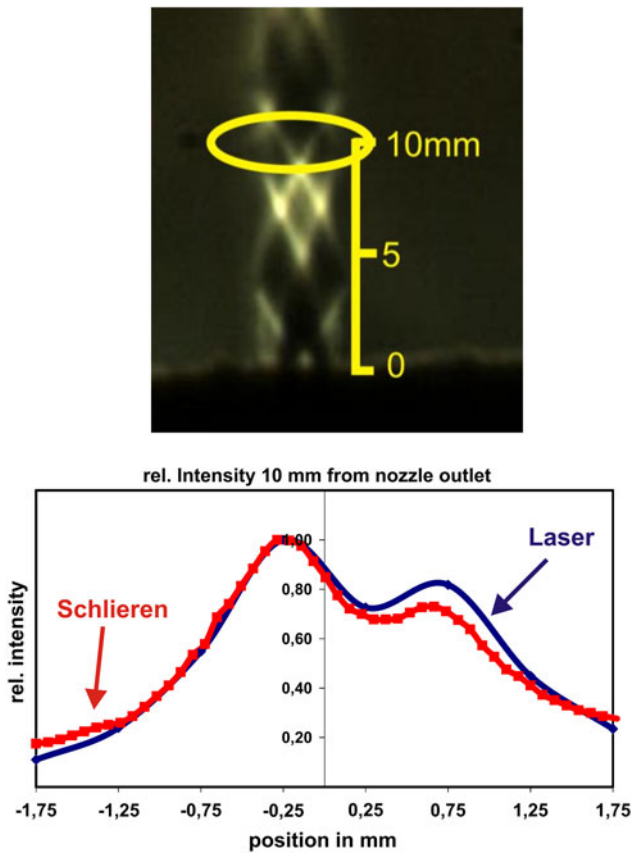

Fig. 10 Relative density distribution (a) complete distribution obtained with Schlieren technique (b) by means of the laser scattering (full line) for a transversal cut at 10 mm, compared to Schlieren technique (dashed line)

6. Limitations

A well-defined allocation of maxima of the same order of interference is not possible if the induced wavelength shift exceeds 25% of the FSR; thus for scattering angles between 10° and 25° and a minimum plate separation of $d = 6.4$ mm the maximum velocities are 3689 m/s (25°) and 8975 m/s (10°) and for a minimum distance of $d = 1.97$ mm 11,981 m/s (25°) and 29,159 m/s (10°), respectively, Fig. 11. Two different points of operation are shown, the solid line for $d = 6.4$ mm and the dashed line for $d = 1.97$ mm.

For a high temperature, and thus low density, flow the scattered Rayleigh spectrum is Gaussian (Ref 6, 15, 25). The width of the scattered spectrum is a function of the square root of gas temperature; thus the FSR $= \lambda^2/(2d)$ is a limiting factor for the maximum temperature of a gas flow to be characterized with the discussed technique. The influence of the temperature to the ratio of FWHM of the scattered spectrum vs the FSR is shown in Fig. 12. For a minimum plate separation of $d = 6.4$ mm (solid line) and a maximum FWHM of 25% of the FSR the maximum temperature to obtain reliable results is 3050 K for argon and 4209 K for air, respectively.

For a reduced minimum plate separation of $d = 1.97$ mm (dashed line) the maximum temperature goes up to $T > 40{,}000$ K.

For scattering perpendicular to the gas flow plane ($\theta = \pi/2$), the ratio of the differential cross section for Rayleigh scattering at bound electrons in non-ionized argon and the differential cross section for Thomson scattering at free electrons is given by (Ref 26):

$$\frac{\frac{d\sigma}{d\Omega}\Big|_{\text{Rayleigh},\,\theta=\pi/2}}{\frac{d\sigma}{d\Omega}\Big|_{\text{Thomson},\,\theta=\pi/2}} = \left(\sum_{\text{trans. } k \to i \text{ Ar0}} \frac{\frac{f_{i\to k}}{\lambda_0^2}}{\frac{1}{\lambda_{k\to i}^2} - \frac{1}{\lambda_0^2}} \right)^2, \qquad \text{(Eq 8)}$$

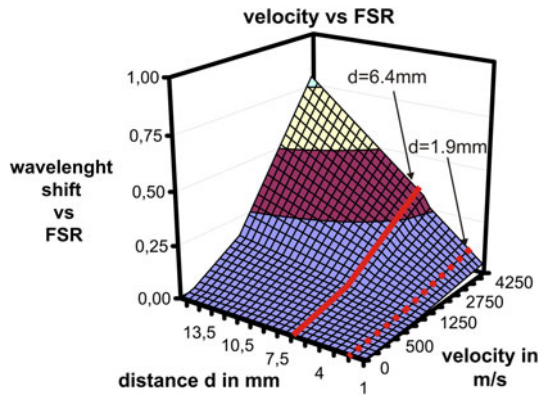

Fig. 11 The ratio of velocity-induced wavelength shift vs. FSR for a scattering angle of 25° as a limiting factor. Two points of operation are shown (a) for a plate separation of $d = 6.4$ mm (full line) and (b) for a plane separation of $d = 1.97$ mm (dashed line)

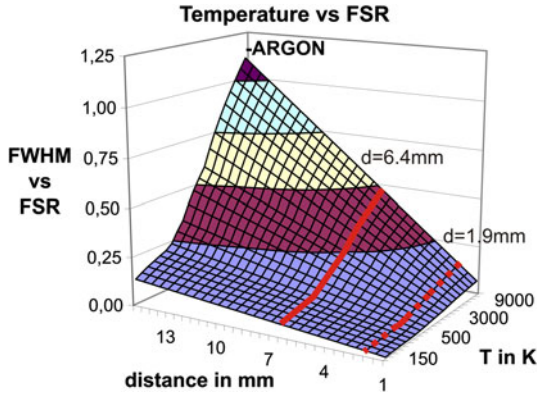

Fig. 12 Ratio of FWHM vs. FSR for argon as a limiting factor. Two points of operation are shown (a) for a plate separation of $d = 6.4$ mm (full line) and (b) for a plane separation of $d = 1.97$ mm (dashed line)

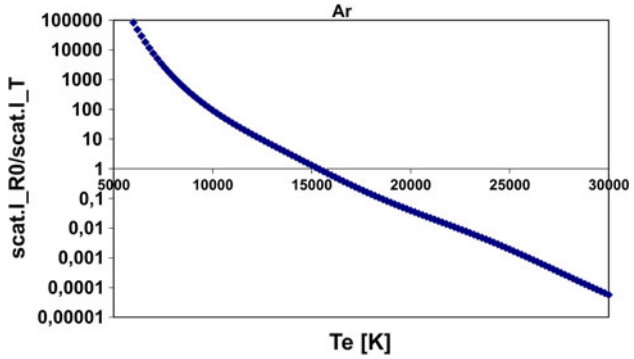

Fig. 13 Rayleigh scattered intensity at non-ionized argon relative to Thomson scattered intensity for an incident laser of 532 nm as a function of the electron temperature in an argon plasma at atmospheric pressure

where λ_0 is the incident laser wavelength, $\lambda_{k \to i}$ is the wavelength for the electron transition in non-ionized argon, and $f_{i \to k}$ is the corresponding oscillator strength. According to the NIST values for non-ionized argon (Ref 27), the quotient above is equal to 231.7 for an incident wavelength of 532 nm. The scattered intensity is proportional to the differential cross section and to the number density of scattering centers: density of argon atoms n_{Ar0} for Rayleigh scattering and density of free electrons n_e for Thomson scattering

$$\frac{I|_{\text{scat. Rayleigh, }\theta=\pi/2}}{I|_{\text{scat. Thomson, }\theta=\pi/2}} = \frac{n_{\mathrm{Ar0}} \frac{d\sigma}{d\Omega}\big|_{\text{Rayleigh, }\theta=\pi/2}}{n_e \frac{d\sigma}{d\Omega}\big|_{\text{Thomson, }\theta=\pi/2}}. \qquad \text{(Eq 9)}$$

Solving Saha's equation, subjected to the electric charge conservation as well as the equation of the ideal gases, the previous quotient is calculated, resulting in a decreasing curve represented in Fig. 13. Above 12,500 K Thomson scattering begins to be no longer negligible and above 15,000 K Thomson scattering is even stronger than Rayleigh scattering.

Hence, both effects (Thomson and Rayleigh scattering) have to be considered which combined lead to a significant number of detected photons at the PO. The distance d between both plates has to be reduced in order to increase the FSR required for diagnostics on thermal plasmas.

7. Conclusion

The developed new technique allows a non-intrusive measurement of the drift velocity as well as a relative density distribution for fast gas flows. The estimation of the velocity without any changes in the optical arrangement allows a fast, stable, and reproducible measurement method. Presently flows with temperatures up to 4000 K (Cold gas spray or high velocity oxy fuel spray) can be measured. In further work, after testing a modified interferometer (decreased plate separation) this technique will be applied to thermal plasma jets to measure the velocity and density distributions.

Acknowledgments

This work was supported in part by the Deutsche Forschungsgemeinschaft (German Research Foundation), Grant SCHE 428/6-2 (PAK 193).

References

1. P. Fauchais, Understanding Plasma Spraying, *J. Phys. D Appl. Phys.*, 2004, **37**, p R86-R108
2. D. Estruch, N.J. Lawson, and K.P. Garry, Application of Optical Measurement Techniques to Supersonic and Hypersonic Aerospace Flows, *J. Aerosp. Eng.*, 2009, **22**, p 383-395
3. I.H. Hutchinson, *Principles of Plasma Diagnostics*, Cambridge University Press, Cambridge, 1987 (Chap. 7)
4. N.A. Clark, Inelastic Light Scattering from Density Fluctuations in Delute Gases: The Kinetic Hydrodynamic Transition in Monatomic Gas, *Phys. Rev. A*, 1975, **12**(1), p 232-244
5. R. Pitz, R. Cattolica, F. Robben, and L. Talbot, Temperature and Density in a Hydrogen-Air Flame from Rayleigh Scattering, *Combst. Flame*, 1976, **27**, p 313-320
6. R.G. Seasholtz, High-Speed Anemometry Based on Spectrally Resolved Rayleigh Scattering, *International Conference on Laser Anemometry*, August 5-9, 1991(Ohio), ASME, EALA, Case Western Reserve University, NASA Lewis Research Center, Ohio Aerospace Institute, NASA Technical Memorandum 104522
7. J.P. Bonnet, D. Gresillon, B. Cabrit, and V. Frolov, Collective Light Scattering as Non-Particle Laser Velocimetry, *Meas. Sci. Technol.*, 1995, **6**, p 620-636
8. R.G. Seasholtz and J. Panda, Rayleigh Scattering for Dynamic Measurement of Velocity and Temperature, AIAA-99-0641, March 2001, NASA/TM 2001-210698
9. A. Koch, "Diagnostik von Plamastrahlen mittels Laserstreuverfahren (Diagnostics of Plasma Flow by Means of Laser Scattering Techniques)," Doctoral Thesis, University of the Federal Armed Forces Munich, 1988 (in German)
10. S.C. Snyder, L.D. Reynolds, G.D. Lassahn, J.R. Finke, and C.B. Shaw, Jr., Determination of Gas-Temperature and Velocity Profiles in an Argon Thermal-Plasma Jet by Laser-Light Scattering, *Phys. Rev. E*, 1993, **47**(3), p 1996-2005
11. G. Forster, "Bestimmung von Parametern thermischer Plasmen mittels Thomsonstreuung (Parameter Determination of Thermal Plasmas by Means of Thomson Scattering)," Doctoral Thesis, University of the Federal Armed Forces Munich 1995 (in German)

12. G. Gregori, J. Schein, U. Kortshagen, J. Heberlein, and E. Pfender, Thomson Scattering Measurements in Atmospheric Plasma Jets, *Phys. Rev. E*, 1999, **49**(2), p 2286-2291
13. A.F. Mielke, ''Development of a Molecular Rayleigh Scattering Diagnostic for Simultaneous Time-Resolved Measurement of Temperature, Velocity and Density,'' Doctoral Thesis, Case Western Reserve University MAE, 2008
14. C.S. Johnson and D.A. Gabriel, *Laser Light Scattering*, Dover Publications, New York, 1994, p 3-29
15. R.B. Miles, W.R. Lempert, and J.N. Forkey, Laser Rayleigh Scattering, *Meas. Sci. Technol.*, 2001, **12**(5), p R33-R51
16. J.-Ph. Perez, *Optik (Optics)*, Spektrum Akademischer Verlag, Berlin, Germany, 1996
17. W. Lochte-Holtgreven and J. Richter, *Quantititative Spectroscopy, Plasma Diagnostics*, North Holland Publishing Co, Amsterdam, 1968, p 296-302
18. G. Hernandez, *Fabry-Perot Interferometers (Cambridge Studies in Modern Optics)*, Vol 3, Cambridge University Press, Cambridge, 1998
19. P.A. Wilksch, Instrument Function of the Fabry-Perot Spectrometer, *Appl. Opt.*, 1985, **24**(10), p 1502-1511
20. J.M. Vaughn, *The Fabry-Perot Interferometer History Theory, Practice and Applications*, Adam Hilger, Bristol, 1989
21. T.A. Hall, Fizeau Interferometer Profiles at Finite Acceptance Angles, *J. Phys. E J. Sci. Instrum.*, 1969, **2**(2), p 837-840
22. T.T. Kajava, H.M. Lauranto, and R.R.E. Salomaa, Fizeau Interferometer in Spectral Measurements, *J. Opt. Soc. Am. B*, 1993, **10**(11), p 1980-1989
23. T.T. Kajava, H.M. Lauranto, and A.T. Friberg, Interference Pattern of the Fizeau Interferometer, *J. Opt. Soc. Am. A*, 1994, **11**(7), p 2045-2054
24. K. Foelsch, The Analytical Design of an Axially Symmetric Laval Nozzle for a Parallel and Uniform Jet, *J. Aeronaut. Sci.*, 1949, p 161-166, 185
25. A.F. Mielke, R.G. Seasholtz, K.A. Elam, and J. Panda, Time-Average Measurement of Velocity, Density, Temperature, and Turbulence Velocity Fluctuations Using Rayleigh and Mie Scattering, *Exp. Fluids*, 2005, **39**(2), p 441-454
26. A.B. Murphy and A.J.D. Farmer, Temperature Measurement in Thermal Plasmas by Rayleigh Scattering, J, *Phys. D Appl. Phys.*, 1992, **25**, p 634-643
27. http://physics.nist.gov/PhysRefData/ASD/lines_form.html